Ultrastrong Coupling of Plasmons and Excitons in a Nanoshell

Adriano Cacciola,[†] Omar Di Stefano,[†] Roberto Stassi,[‡] Rosalba Saija,[†] and Salvatore Savasta*[,†]

[†]Dipartimento di Fisica e di Scienze della Terra, Università di Messina, Viale F. Stagno d'Alcontres 31, I-98166 Messina, Italy and [‡]Dipartimento di Fisica e Chimica, Group of Interdisciplinary Physics, Universit and CNISM, Viale delle Scienze, Edificio 18, I-90128 Palermo, Italy

ABSTRACT The strong coupling regime of hybrid plasmonic–molecular systems is a subject of great interest for its potential to control and engineer light–matter interactions at the nanoscale. Recently, the so-called ultrastrong coupling regime, which is achieved when the light–matter coupling rate reaches a considerable fraction of the emitter transition frequency, has been realized in semiconductor and superconducting systems and in organic molecules embedded in planar microcavities or coupled to surface plasmons. Here we explore the possibility to achieve this regime of light–matter interaction at nanoscale dimensions. We demonstrate by accurate scattering calculations that this regime can be reached in nanoshells constituted by a core of organic molecules surrounded by a silver or gold shell. These hybrid nanoparticles can be exploited for the design of all-optical ultrafast plasmonic nanocircuits and -devices.

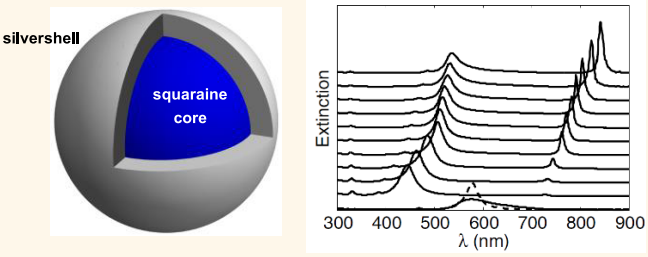

KEYWORDS: localized surface plasmons · plexcitons,nanoshell · polaritons · ultrastrong coupling

The interaction of quantum emitters as quantum dots or dye molecules with individual metallic nanostructures has been attracting increasing attention since it carries significant potential for manipulating light on the nanoscale.[1−11] The formation of hybrid nanostructures between metallic nanoparticles and organic dyes can lead to the development of novel nanoscale plasmonic devices and nanocircuits[12] like ultrafast switches and modulators,[13] single-photon transistors,[14] and nanolasers.[15,16] Localized surface plasmons (LSPs) supported by metallic nanostructures are able to focus, trap, and guide optical energy into subwavelength spatial regions;[17] hence, they can be exploited as nanoscale resonators and waveguides.[18] On the other hand, plasmonic nanostructures exhibit only weak nonlinearities preventing saturation and active control. Coupling LSPs to nonlinear optical resonances such as excitons in molecular or semiconducting nanostructures can provide the missing nonlinearity and gain.[19,20]

In the context of light–matter coupling, when the interactions between electronic transitions and photonic or plasmonic modes overcome radiative and nonradiative losses, the system enters the strong coupling regime where the energy is coherently and reversibly exchanged between the emitter and the electromagnetic field. This regime gives rise to new hybrid quasiparticles which can have unusual properties possessed by neither original particle. This nonperturbative regime allows for studies of fundamental quantum features like entanglement and decoherence,[21] as well as for exploration of potential applications like quantum information processing. Strong coupling at optical frequencies was first observed for atoms passing through a high finesse microcavity and then demonstrated in the solid state in a variety of systems ranging from semiconductor quantum structures to cavity embedded organic molecules and superconducting quantum circuits.[22]

Coherent coupling and electromagnetic transparency of quantum emitters interacting with surface plasmon–polaritons[23−27] or with LSP modes in individual nanometric-size complexes has been demonstrated.[1,2,8−11] However, true strong coupling requires that the vacuum Rabi splitting $2\Omega_R$ be larger than the dissipative broadening of both the emitter and the light-mode γ_0 and γ_c, respectively. More precisely at resonance the broadening of the polariton peaks as seen, *e.g.*, in absorption measurements is given by $\gamma_p = (\gamma_0 + \gamma_c)/2$, and a complete

* Address correspondence to ssavasta@unime.it.

Received for review August 19, 2014 and accepted October 22, 2014.

Published online October 22, 2014
10.1021/nn504652w

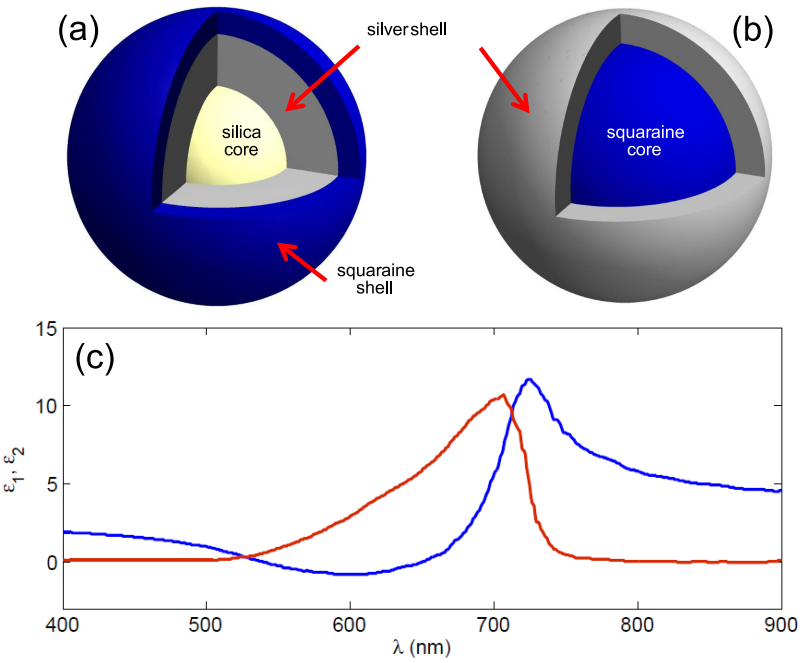

Figure 1. (a) A sketch showing (a) the silica core surrounded by the squaraine shell and by the external metallic shell and (b) the nanoshell constituted by a squaraine core surrounded by a metal (silver or gold) shell. (c) Real (blue line) and imaginary (red) part of the complex relative dielectric function of a solid film of pure squaraine molecules.

splitting, corresponding to the possibility to observe reversible and coherent energy exchange between excitons and the light mode in the time domain, is obtained for $2\Omega_R \gg \gamma_p$. Nonetheless, thanks to small mode volumes and strong molecular dipole moments, remarkable splitting values $2\Omega_R$ (up to ~400 meV in dimer structures[10]) have been achieved in nanoscale hybrid systems; true strong coupling with complete splitting has only been approached.[8] This is a consequence of the very large dissipative broadening of plasmonic resonances. Usually, in these systems, the following inequality holds: $\gamma_c > 2\Omega_R \geq \gamma_0$. In this intermediate regime, the splitting is better described as a transparency dip (exciton-induced transparency regime) or by a Fano-like resonance describing the interaction of a narrow resonance (the exciton) with a broad one (the LSP resonance). A pronounced 50% transparency dip has been recently observed.[8] These results and predictions of electromagnetically induced transparency (EIT) and vacuum Rabi splitting in dimer nanoantennas interacting with single quantum dots[3−5] have indicated exciting possibilities for room-temperature nanoscale cavity quantum electrodynamics (cQED) and quantum optics applications contributing to the rapidly growing field of quantum plasmonics.[28]

Recently, a new regime of cavity quantum electrodynamics (QED), where the light−matter coupling rate becomes an appreciable fraction of the unperturbed resonance frequency of the system, has been experimentally reached in a variety of solid state systems.[26,29−34] In this so-called ultra strong coupling (USC) regime, the routinely invoked rotating wave approximation is no longer applicable and the antiresonant terms significantly change the standard cavity-QED scenarios.[35−38] A puzzling property of these systems is that their ground state is a squeezed vacuum containing correlated pairs of photons and material excitations. The USC between organic molecules and surface plasmon polaritons has been demonstrated by covering a periodic plasmonic structure with the organic molecules.[26]

By employing accurate scattering calculations based on a generalization of the Mie theory implemented within the T-matrix formalism,[39] we show that the USC regime can be reached in nanoshells constituted by a core of organic molecules surrounded by a silver or gold shell (see Figure 1b). Because of its large energy-integrated absorption coefficient, we consider a core constituted by only squaraine dye molecules (100% squaraine core). A planar microcavity embedded p−i−n monolithic light emitting diode working in the USC regime, employing a thin film of squaraine dye as active layer, has been recently reported.[34] We also investigate a second nanoshell structure constituted by a silica core, a silver shell, and an external 100% squaraine layer (see Figure 1a). We find that a giant vacuum Rabi splitting of the order of $2\Omega_R \simeq 0.78$ eV can be obtained resulting in a remarkable normalized coupling rate $2\Omega_R/\omega_0 \approx 42\%$, where $\hbar\omega_0$ is the exciton energy.

RESULTS AND DISCUSSION

The wavelength dependence of the real and imaginary part of the complex relative dielectric function

$\varepsilon_{sq} = \varepsilon_{sq1} + i\varepsilon_{sq2}$ for a pure squaraine solid film obtained from the experimental optical constants determined by variable angle spectroscopic ellipsometer[40] is shown in Figure 1c. The experimental data showed slightly anisotropic properties that we here neglect. The displayed dielectric function describes the optical response along the horizontal directions. Previous studies on organic polaritons and plexcitons have focused principally on materials exhibiting narrow line widths and high peak absorbance such as J-aggregates and porphyrins. However, broad optical transitions can often possess much larger oscillator strengths and thus be advantageous for reaching the USC regime.[26,33,34] The imaginary part of the dielectric function in Figure 1c shows that solid films of pure squaraine molecules display a very broad absorption line. This inhomogeneously broadened absorption line arises from direct transitions from the ground state to different vibrational excited states. The strong coupling in the presence of inhomogeneously broadened absorption lines has been investigated theoretically by Houdré *et al.*[41] They showed that the vacuum Rabi splitting depends on the energy-integrated absorption rather than on just the absorption peak. Moreover, for a vacuum Rabi splitting significantly larger than the inhomogeneous broadening, the line width of the polariton peaks results to be homogeneously broadened. Hence, coherent light−matter coupling can be achieved even in the presence of strong inhomogeneous broadening, if the light−matter coupling rate is sufficiently strong. In all subsequent calculations, the frequency-dependent dielectric permittivity of silver and gold is taken from ref 42. The details of the here exploited theoretical and numerical framework are described in the Methods section. All the numerical calculations displayed in the paper consist of extinction cross section spectra.

We start investigating the system sketched in Figure 1a consisting of a spherical silica core covered with a thin, uniform metal layer finally covered by a r_{sq} = 5 nm layer of dye molecules. This shell configuration has been exploited in previous studies on plexcitons based on nanoshell−J-aggregate complexes. When the core size/shell thickness ratio varies, the plasmon energies of the nanoparticle can be systematically modified, and can be tuned through the exciton energy of the dye molecules. Figure 2 displays the extinction cross sections for nanoshell−squaraine complexes with total radius r_t = 40 nm. From top to bottom, the silica core radius/silver shell thickness is 31/4 (green), 30/5 (red), 29/6 (blue). The dashed lines describe the corresponding cross sections in the absence of the squaraine layer and provide direct information on the resonance frequency ω_c of the effective cavity constituted by the nanoshell. The figure does not show in a clear way those features as the anticrossing and Lorentzian-like splitted peaks which are

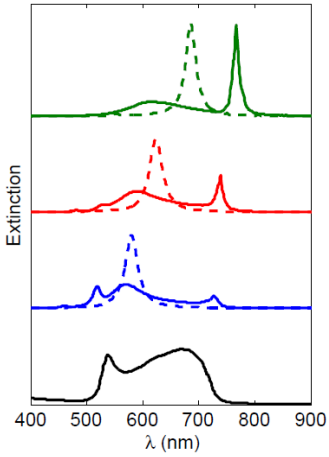

Figure 2. Extinction cross section spectra obtained for the system sketched in Figure 1a consisting of a spherical silica core covered with a thin, uniform metal layer finally covered by a 5 nm layer of dye molecules with total radius r_t = 40 nm. The different spectra have been obtained by changing the silica core radius/silver shell thickness (see text). The dashed lines describe the corresponding cross sections in the absence of the squaraine layer. The bottom black line describes the extinction cross section in the absence of the silver layer (silica core radius 35 nm, r_{sq} = 5 nm).

the signature of light−matter coherent coupling. The origin of this odd behavior can be understood looking at the bottom black line in Figure 2 describing the extinction cross section in the absence of the silver layer (silica core radius 35 nm, r_{sq} = 5 nm). Such spectrum, which describes the response of the matter system, is characterized by a very broad structure with two asymmetric peaks which prevents a true coherent coupling in the presence of the silver shell. This extinction spectrum resembles the corresponding ones obtained for gold nanoshells and can be interpreted as due to the interaction between the outer and inner localized surface polaritons in the shell,[43] determined by the strong dipole moment of squaraine molecules. Analogous results are obtained replacing silver with gold. Hence, these calculations shows that the strong and broad squaraine absorption line prevents the achievement of a clear light−matter coherent coupling in contrast to what has been obtained with squaraine based planar microcavities or in previous studies on nanoshells covered with materials exhibiting narrow line widths. Analogous results, here not shown, are obtained replacing the squaraine layer with merocyanine molecules which have been successfully employed to achieve the ultrastrong coupling regime at optical frequencies in planar microcavities and in plasmonic periodic structures.[26]

In the search for ultrastrong light−matter coupling in a single plasmonic nanostructure, we investigated a second core−shell complex (see Figure 1b) constituted by a squaraine core of radius r_{sq} surrounded by a silver or gold shell. Figure 3a shows the extinction cross section spectra for squaraine−silver core−shell

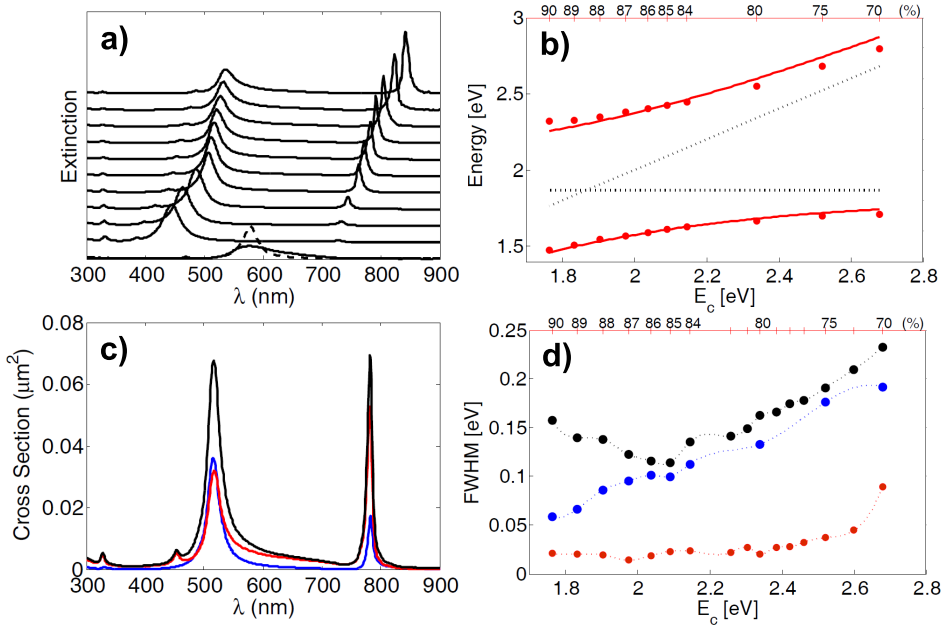

Figure 3. (a) Extinction cross section spectra for squaraine−silver core−shell structures with total radius r_t = 40 nm. When the percentage of the metal shell thickness $\alpha = 100 \times r_{sq}/r_t$ is changed, it is possible to tune the plasmonic resonance, across to the squaraine absorption line. Extinction spectra for α ranging from 90% to 70% (from top to bottom) are displayed. The bottom dashed line describes the extinction cross section in the absence of the silver layer (silica core radius 35 nm, r_{sq} = 5 nm); the bottom black full line describes the extinction spectrum of the nanoshell in the absence of the excitonic resonance. The corresponding energy peaks, reported in (b) as a function of the plasmonic resonance (red full circles), show a clear anticrossing behavior. The dotted lines describes the nanoshell plasmonic resonance in the absence of the exciton resulting from the fit with the analytic formula describing the polariton energies in the USC regime (see text for details). The continuous red lines describe the analytical polariton energies which correspond to the eigenvalues of the Hopfield Hamiltonan used to fit the data with ω_0 and g as fitting parameters. (c) A single extinction spectrum (black line) for the squaraine−silver core−shell structure and the corresponding scattering (blue line) and absorption (red line) cross sections obtained for α = 0.86. (d) Line widths (fwhm) as a function of α of the lower (red circles) and upper (black circles) polariton lines and of the plasmonic resonances (in the absence of the exciton resonance) (blue circles) for the squaraine−silver core−shell structures.

structures with total radius r_t = 40 nm. When the percentage of the metal shell thickness 100 − α where $\alpha = 100 \times r_{sq}/r_t$ is changed, it is possible to tune the plasmonic resonance frequency ω_c, across the squaraine absorption line. In Figure 3a cross sections for α ranging from 90% to 70% (from top to bottom) are displayed. For reference, we also included in Figure 3a (bottom lines) the extinction cross section for a 40 nm only squaraine sphere (black continuous line) and the extinction cross section for a core−shell system with α = 84% in the absence of the excitonic resonance (dashed-line). The latter calculation has been carried out replacing the squaraine dielectric function with the estimated high-frequency (at $\lambda \approx 400$ nm) squaraine dielectric function $\varepsilon_h = 2.5$. We observe that, in contrast to the extinction spectrum of the squaraine nanoshell (bottom line in Figure 2), the extinction spectrum for the 40 nm only squaraine sphere (black continuous line) displays a simpler structure with a quite broad peak at about λ = 580 nm significantly blue-shifted with respect to the peak of the imaginary part of the dielectric function shown in Figure 1c. This shift is not unexpected since in the quasi-static approximation[44] the extinction cross section can display resonances when $\varepsilon_1 + 2\varepsilon_b$ reaches a minimum, where ε_b is the dielectric function of the medium sourrounding the individual system. We used for all the calculations in this paper ε_b = 1. The energy peaks of the extinction cross section spectra for the squaraine−silver core−shell structures are reported in Figure 3b which shows a clear anticrossing behavior of the plexciton peaks as a function of the plasmonic resonance. This panel has been obtained by plotting the plexciton peaks from Figure 3a *versus* α (upper horizontal axis) and *versus* the nanoshell plasmonic resonances in the absence of the excitonic resonance reported on the bottom horizontal axis. These LSP resonances (in the absence of the excitonic transition) have been calculated as the dashed spectrum in Figure 3a, replacing the squaraine dielectric function with the estimated high-frequency squaraine dielectric permittivity. Figure 3a shows two greatly splitted plexciton (polariton) peaks with a complete (∼100%) transparency dip. Figure 3b shows a huge Rabi splitting and a wide polariton energy-gap where no cavity-polariton solutions can be found, which is an USC signature and cannot be described with a coupled oscillator model in the rotating wave approximation.[30] Specifically, in the limit $\omega \ll \omega_0$, the upper curve in Figure 3b tends to an asymptotic value ≈2.3 eV, and in the opposite limit $\omega_c \gg \omega_0$, the lower curve tends to a different asymptotic value ≈1.7 eV, where $\hbar\omega_0$ is the exciton energy and $\hbar\omega_c$ is the

resonance energy of the LSP mode. These two asymptotic values define a polariton gap where no plexciton peaks can appear independently on the tuning of the plasmonic resonance. As discussed in ref 8, this gap has its origin in the quadratic and antiresonant terms of the light−matter interaction Hamiltonian. As a consequence, the observation of a polaritonic gap in the dispersion curve can be taken as a signature of the ultrastrong coupling regime. Figure 3 demonstrates that the core/shell (squaraine/silver) structure sketched in Figure 1b can be exploited for the realization of single hybrid nanoparticles supporting exciton−plasmon ultrastrong coherent coupling. It is useful to compare these numerical results, derived with a generalization of the Mie theory, with the Hopfield model which takes into account the antirotating terms. The latter is a quantum theory of two coupled harmonic oscillators (the exciton and the photon mode). The polariton energies can be described analytically by the eigenvalues of the Hopfield Hamiltonian of the interacting system[30,45,46] which are solutions of the following equation,

$$(\omega^2 - \omega_c^2)(\omega^2 - \omega_0^2) - \omega_0^2 g^2 \omega^2 = 0 \qquad (1)$$

where $g = 2\Omega_R/\omega_0$ is the normalized coupling factor. The solutions of eq 1 give the lower and the upper polariton dispersion energies of the corresponding eigenstates of the Hopfield Hamiltonian. The continuous lines in Figure 3b are the result of the best fit of the data with the analytical solutions of eq 1 where we have used as free parameters the exciton energy and the normalized coupling factor. We obtained $\hbar\omega_0 = 1.868$ eV and $g = 0.42$ eV, corresponding to a vacuum Rabi splitting $2\hbar\Omega_R \simeq 0.78$ eV. The agreement is quite good; some discrepancy between the data and the fit can be observed however for the upper polariton. These differences are expected since the Hopfield model, in contrast to the present case, refers to a single exciton line and neglects the influence of damping. We attribute such discrepancies in the upper polariton curve mainly as due to the strong inhomogeneous broadening at short wavelengths (see the imaginary part of the squaraine dielectric function in Figure 1c). In Figure 3b, we also plotted for reference the exciton energy obtained from the fit (horizontal dotted line) together with the nanoshell plasmonic resonance $\omega_p(\alpha)$ in the absence of the excitonic resonance which has been obtained replacing the squaraine dielectric function with the estimated high-frequency (at $\lambda \approx 400$ nm) squaraine dielectric function $\varepsilon_h = 2.5$. These two dotted lines describe the crossing excitonic and plasmonic resonances in the absence of interaction. It is worth noticing that the exciton energy obtained from the fit is close to the peak energy of the imaginary part of the squaraine dielectric function rather than to the blue-shifted extinction peak of the 40 nm squaraine sphere. This result shows that the presence of the metallic nanoshell, which focuses on the squaraine core the incoming plane wave, strongly modifies the scattering process.

While Figure 3a displays only extinction spectra, in Figure 3c we also reported, in addition to the extinction spectrum (black line), the scattering cross section (blue line) and the absorption (red line) obtained for $\alpha = 0.86$. For the size here considered, we observe that the absorption and the scattering contributes almost equally to the extinction spectrum. In the absorption (and of course extinction) spectrum, two small peaks at lower wavelengths are clearly visible. The small peak at higher wavelength originates from higher order multipole plasmonic contributions (we verified that dropping in the calculation multipolar terms or reducing the size this peak disappears). The peak at lower wavelength can be attributed to the higher energy antibonding plasmon present in plasmonic nanoshells.[43]

Figure 3d displays the line widths (fwhm) of the lower (red circles) and upper (black circles) polariton lines and of the plasmonic resonances (in the absence of the exciton resonance) (blue circles). As expected, the line width of the plasmonic resonance grows with the increase of the thickness of the silver shell (corresponding to a decrease of α) due to increasing plasmonic losses. The dependence of the polariton line widths is not trivial and it is affected by several factors such as the dependence of the exciton and photon content on the exciton−plasmon energy detuning, the variation of the excitonic and plasmonic losses as a function of α, the dependence of the imaginary part of the Ag dielectric function on frequency, and the presence of a very large inhomogeneously broadened excitonic line. Despite the broad inhomogeneous excitonic absorption line of the squaraine solid film (see Figure 1c and the bottom continuous line in Figure 3a), Figure 3c shows a lower polariton line width significantly narrower than both those of the plasmon mode and of the exciton absorption line. This feature can be ascribed to the collective coupling of the inhomogeneous excitons with the plasmon mode, which can result in a system that behaves like a single homogeneous exciton with a very strong oscillator strength coupled coherently with the surface plasmon mode.[41] Specifically, it has been shown that, when the Rabi splitting is larger than the inhomogeneus line width, the polariton line widths are approximately given by half the sum between the cavity line width and the homogeneous exciton line width. This analysis explains the quite narrow plexciton line widths observed in Figure 3a, despite the broad exciton and plasmon lines.[41] On the contrary, when the Rabi splitting approaches the inhomogeneous broadening, at resonance the polariton line widths are approximately given by half the sum between the cavity line width and the inhomogeneous exciton line width.[41] Such increase of coherence when increasing the exciton−photon coupling in the presence of inhomogeneously broadened excitons has been observed directly in the time domain in cavity-embedded

semiconductor multiple quantum wells by time-resolved coherent reflectivity spectroscopy.[47] Hence, with such a large coupling strength it is possible to undress the exciton homogeneous line width from its inhomogeneous broadening, which allows for plexcitons with unprecedented narrow emission lines and coherence times. This result suggests that the ultrastrong coupling regime can be exploited to obtain narrow emission lines, highly desired for many applications, despite the presence of broad exciton and plasmon lines. It is worth noticing, however, that the upper polariton line width is always larger than the lower one. This behavior can be mainly ascribed to the strong asymmetric line shape of the excitonic absorption line (see, *e.g.*, the imaginary part of the squaraine dielectric function in Figure 1) displaying a quite long tail at shorter wavelengths. An analogous behavior has been observed for squaraine-based microcavity polaritons.[48] It is also interesting to observe that the fwhm of the upper polariton reaches a minimum close to the minimum splitting, while for $\alpha \geq 86\%$ being the upper polariton mainly plasmon-like, it follows the line width of the plasmonic resonances.

Usually, dye-molecules based spherical cores or nanoshells are realized with a structural supporter like dye-doped silica (see, *e.g.*, ref 15). Of course in this case, the concentration of dye molecules drops well below 100%. To face this design possibility, we performed some calculations considering a silica core containing the squaraine dye molecules. The optical properties of squaraine molecules diluted in a solid host matrix can differ significantly from those of 100% squaraine films. Specifically, as the squaraine molecules are somewhat far from each other, the resulting absorption spectrum is similar to that of the diluted liquid solution, while for 100% squaraine films, the stronger intermolecular interaction results in a larger exciton energy distribution.[48] Figure 4a shows the dielectric function of a film obtained diluting 10% in volume squaraine molecules into an NPB matrix.[48] They have been obtained by the measured absorbance[48] by means of a Kramers–Kronig procedure.[49] We can consider it as the average dielectric function. If we apply the Bruggeman formula,[50] it is possible to extract the ideal pure squaraine dielectric function in the absence of intermolecular interaction. The latter can be inserted in the Bruggeman formula in order to get the average dielectric function in the case of different matrices and/or concentrations. In this way, we obtained the average dielectric functions for a squaraine-doped silica core with different doping concentrations. Figure 4b compares the extinction spectrum for a 100% squaraine core (as in Figure 3a) with spectra obtained with a core with squaraine volume concentrations of 80% (green line) and 40% (red line). All the three spectra have been calculated using $\alpha = 88\%$. The vacuum Rabi splitting reduces significantly even for the higher concentration; however, the splitted polariton peaks remain well

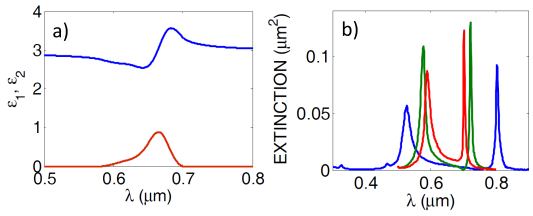

Figure 4. (a) Dielectric function of a film obtained diluting 10% in volume squaraine molecules into an NPB matrix. It has been obtained from the experimental optical density (see text). (b) Comparison of the extinction spectrum for a 100% squaraine core (as in Figure 3a) with spectra obtained with a core with squaraine volume concentrations of 80% (green line) and 40% (red line). All the three spectra have been calculated using $\alpha = 88\%$.

separated. The lower splitting, compared to that of the full squaraine-core sample, is due to different reasons: (i) the lower squaraine concentration; (ii) the larger squaraine exciton energy distribution of the 100% squaraine films determines a higher integrated optical density; (iii) the optical constants used for calculations with the 100% squaraine core have been taken from ref 40 where samples with a slightly higher optical density with respect to samples in ref 48 have been realized.

Figure 5 displays analogous calculations as in Figure 3 but with the silver shell replaced by gold. The obtained results show that the ultrastrong coupling regime can be also obtained with a squaraine/gold core/shell with subwavelength dimensions. The obtained splitting is however somewhat smaller. By fitting the data with the solutions of eq 1, we obtain a normalized coupling factor $g = 0.348$, somewhat lower than that obtained with the silver core. The upper and lower polariton curves obtained from the fit are dispalyed as continuous lines in Figure 5b. This panel shows that for higher plasmonic resonance frequencies, corresponding to $\alpha < 70\%$, the anticrossing behavior of the upper polariton peaks tend to disappear and the upper polariton branch becomes quite flat. This effect can be ascribed to the relevant increase of plasmonic losses when increasing the thickness of the gold shell. In Figure 3c, we also reported, in addition to the extinction spectrum (black line), the scattering cross section (blue line) and the absorption (red line) obtained for $\alpha = 0.86$. For the sized here considered, we observe that for the gold/squaraine complex the absorption cross section is larger than that of scattering, owing to the larger plasmonic losses of gold with respect to silver.

Figure 5d displays the line widths (fwhm) of the lower (red circles) and upper (black circles) polariton lines and of the plasmonic resonances (in the absence of the exciton resonance) (blue circles). As expected, the line width of the plasmonic resonance grows rapidly with the increase of the thickness of the gold shell (corresponding to a decrease of α) due to increasing plasmonic losses. Also in this case the line width of the lower

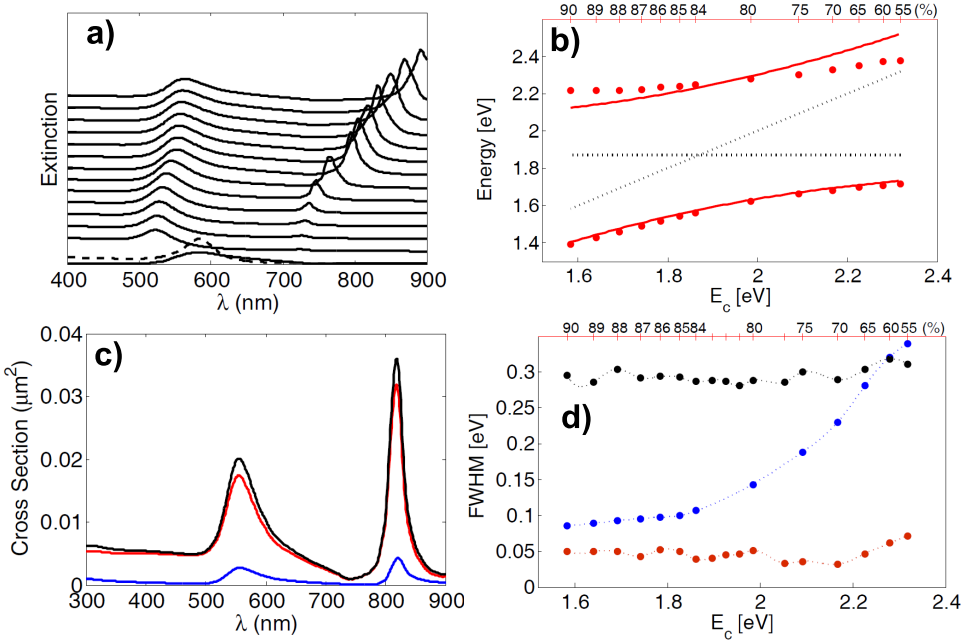

Figure 5. (a) Extinction cross section spectra for squaraine–gold core–shell structures with total radius r_t = 40 nm. When the percentage of the metal shell thickness $\alpha = 100 \times r_{sq}/r_t$ is changed, it is possible to tune the plasmonic resonance, accoss the squaraine absorption line. Extinction spectra for α ranging from 90% to 55% (from top to bottom) are displayed. The corresponding energy peaks, reported in (b) as a function of the plasmonic resonance (red full circles), show a clear anticrossing behavior. Panel b also displays for reference the exciton energy obtained from the fit (horizontal dotted line) together with the nanoshell plasmonic resonance $\omega_p(\alpha)$ in the absence of the excitonic resonance. The continuous red lines describe the analytical polariton energies which correspond to the eigenvalues of the Hopfield Hamiltonan used to fit the data with and g as fitting parameters. In this case, ω_0 has been fixed by the fit for the nanoshell with the silver core (see Figure 3b). (c) A single extinction spectrum (black line) for the squaraine–gold core–shell structure and the corresponding scattering (blue line) and absorption (red line) cross sections obtained for α = 0.86. (d) Line widths (fwhm) as a function of α of the lower (red circles) and upper (black circles) polariton lines and of the plasmonic resonances (in the absence of the exciton resonance) (blue circles) for the squaraine–gold core–shell structures.

polariton resonances is narrower than that of the upper polariton and of the plasmonic resonance. Figure 5d also shows that the upper polariton line width undergoes only small changes with α. This could be ascribed to the flatness of the upper polariton dispersion curve.

CONCLUSIONS

By accurate scattering calculations, we investigated the possibility to achieve the light–matter ultrastrong coupling regime at nanoscale dimensions. We demonstrated that this regime can be reached in nanoshells constituted by a core of organic molecules surrounded by a silver or gold nanometric shell. Despite the very broad exciton line, quite narrow and well separated plexciton peaks can be obtained. On the contrary, we showed that the usually adopted core–shell configuration with a final shell of organic material in this case does not work owing to the very high absorption coefficient of squaraine, which, on the other hand, is a key feature for obtaining ultrastrong coupling. Electroluminescence of squaraine based polaritons has been recently demonstrated in planar microcavities with metal mirrors.[34] Of particular interest for the development of ultracompact light sources with high color purity are the here reported very narrow lower polariton line widths, since light emission from organic molecules in the strong coupling regime occurs at the lower polariton peak.[34,48] We expect that analogous results can be obtained employing other organic materials with very large absorption as those already exploited to reach the ultrastrong coupling regime in conventional planar microcavities.[26,33] These ultracompact hybrid nanoparticles can be exploited for the design of novel all-optical ultrafast plasmonic nanocircuits and -devices. The very high splitting and transparency dip promised by these nanocomplexes can also be exploited for the demonstration of high efficiency laser cooling of the center-of-mass motion of hybrid nanostructures.[51]

METHODS

Model and Computational Approach. To calculate the optical properties of the nanoshell, we extend the Mie theory to radially nonhomogeneous spheres. We assume that all the fields depend on time through the factor $\exp(-i\omega t)$ and define the propagation constant in vacuo $k_v = \omega/c$. As we will shown below, this approach allows us to perform a multipole expansion not only of the incident and scattered field but also of the internal one. The propagation constant of the

homogeneous, no absorbing and isotropic surrounding medium is $k = nk_v$, where n is refractive index. The incident field is the plane wave

$$\mathbf{E}_I = E_0\hat{\mathbf{e}}\exp[i\mathbf{k}_I\cdot\mathbf{r}] \quad (2)$$

where $\hat{\mathbf{e}}$ is the unit polarization vector and $\mathbf{k}_I = k\hat{\mathbf{k}}_I$ is the propagation vector. We consider a radially nonhomogeneous sphere with radius ρ and complex refractive index $n_0 = n_0(r)$. In the region external to the sphere, the field is the superposition of E_I, eq 2, and of the scattered field E_S. Both fields are expanded in a series of spherical vector multipole fields. We define the vector multipole fields H as[52]

$$\begin{aligned}\mathbf{H}^{(1)}_{lm}(\mathbf{r}, K) &= h_l(Kr)\mathbf{X}_{lm}(\hat{\mathbf{r}})\\ \mathbf{H}^{(2)}_{lm}(\mathbf{r}, K) &= \frac{1}{K}\nabla\mathbf{H}^{(1)}_{lm}(\mathbf{r}, K)\end{aligned} \quad (3)$$

where X_{lm} are vector spherical harmonics,[53] h_l are spherical Hankel functions of the first kind, and superscripts (1) and (2) refer to the values of parity index p appropriate to the magnetic and electric multipoles, respectively. The H multipole fields satisfy the radiation condition at infinity. We also define the multipole fields J that are regular at the origin: they are identical to the H-fields except for the substitution of the spherical Bessel functions j_l in place of the Hankel functions h_l. We expand the electric fields outside the sphere as

$$\boldsymbol{E}_{ext} = \boldsymbol{E}_S + \boldsymbol{E}_I = E_0\sum_{plm}[A^{(p)}_{lm}\mathbf{H}^{(p)}_{lm}(\mathbf{r}, k) + W^{(p)}_{lm}\mathbf{J}^{(p)}_{lm}(\mathbf{r}, k)] \quad (4)$$

where the amplitudes of the incident field $W^{(p)}_{lm}$ are defined by ref 39, and the amplitudes $A^{(p)}_{lm}$ are determined by the boundary conditions at the surface of the scattering sphere. Since it does not imply any far-field approximation, expansion 4 is valid everywhere outside the sphere.

Both the internal electric and magnetic fields do not satisfy the customary Helmholtz equation, but rather the equations

$$\begin{aligned}\nabla\nabla\boldsymbol{E} - n_0^2(r)k_v^2\boldsymbol{E} &= 0\\ \nabla\nabla\boldsymbol{B} - n_0^2(r)k_v^2\boldsymbol{B} &= -ik_v\nabla n_0^2(r)\boldsymbol{E}\end{aligned} \quad (5)$$

that are coupled because of the assumed nonhomogeneity of the material. Nevertheless, thanks to the spherical symmetry of the scatterer, the internal field can still be expanded in a series of vector spherical harmonics in the form[54,55]

$$\boldsymbol{E}_T = \sum_{lm}\left[C^{(1)}_{lm}\Phi_l(r)\boldsymbol{X}_{lm}(\hat{\mathbf{r}}) + C^{(2)}_{lm}\frac{1}{n_0^2}\frac{1}{k_v}\nabla\Psi_l(r)\boldsymbol{X}_{lm}(\hat{\mathbf{r}})\right] \quad (6)$$

$$i\boldsymbol{B}_T = \sum_{lm}\left[C^{(1)}_{lm}\frac{1}{k_v}\nabla\Phi_l(r)\boldsymbol{X}_{lm}(\hat{\mathbf{r}}) + C^{(2)}_{lm}\Psi_l(r)\boldsymbol{X}_{lm}(\hat{\mathbf{r}})\right] \quad (7)$$

that, for any choice of the radial functions and for any radial dependence of the refractive index, satisfies the Maxwell equations $\nabla B = 0$ and $\nabla n_0^2\boldsymbol{E} = 0$. The equations

$$\begin{aligned}\left[\frac{d^2}{dr^2} - \frac{l(l+1)}{r^2} + k_v^2n_0^2 - \frac{2}{n_0}\frac{dn_0}{dr}\frac{d}{dr}\right](r\Psi_l(r)) &= 0\\ \left[\frac{d^2}{dr^2} - \frac{l(l+1)}{r^2} + k_v^2n_0^2\right](r\Phi_l(r)) &= 0\end{aligned} \quad (8)$$

are derived by substituting eqs 6 and 7 into eq 5. The solutions to these equations are the radial functions $\Psi_l(r)$ and $\Phi_l(r)$ regular at the origin. The eqs 8 are integrated numerically. When $n_0(r)$ reduces to a constant, $\Phi_l = \Psi_l = j_l(n_0k_vr)$.

When we impose the customary boundary conditions across the surface of the sphere, the mutual independence of the vector spherical harmonics yields, for each l and m, four equations among which the amplitudes of the internal field $C^{(p)}_{lm}$ can be easily eliminated. We then get the amplitudes of the scattered field in the form

$$A^{(p)}_{lm} = -R^{(p)}_l W^{(p)}_{lm} \quad (9)$$

with

$$R^{(p)}_l = \frac{G^{(p)'}_l(x)u_l(x) - (1+\bar{n}\delta_{p2})^2G^{(p)}_l(x)u'_l(x)}{G^{(p)'}_l(x)w_l(x) - (1+\bar{n}\delta_{p2})^2G^{(p)}_l(x)w'_l(x)} \quad (10)$$

where $x = k\rho$, $= (n_0(\rho)/n) - 1$ and

$$G^{(1)}_l(kr) = kr\Phi_l(r), \quad G^{(2)}_l(kr) = kr\Psi_l(r) \quad (11)$$

Once the amplitudes $A^{(p)}_{lm}$ have been calculated, the amplitudes $C^{(p)}_{lm}$ are derived and thus the field at any point inside the sphere.

To preserve the continuity of the refractive index and its radial derivative between two contiguous layers, a thin transition layer is placed at the interface. In this layer, defined by the radial interval $r_- \le r \le r_+$, the refractive index varies from n_- to n_+ according to the rule

$$n_0^2(r) = n_-^2 + (3s^2 - 2s^3)\Delta \quad (12)$$

where we define the quantities

$$\Delta = n_+^2 - n_-^2, \quad s = \frac{r - r_-}{r_+ - r_-} \quad (13)$$

Provided the transition layer is thin enough, the scattering properties of the sphere are not altered.[55] Moreover, such a transition layer improves the numerical convergence expecially in the presence of boundaries with very different optical constants. The introduction of a transition layer of appropriate thickness may also account for the fact that the external layer is actually formed by successive deposition of atoms and molecules. It is reasonable to think that the first deposited atoms are adsorbed at the surface of the internal layer, thus giving origin to a smooth transition from the properties of the internal layer to those of the external layer in formation.

Conflict of Interest: The authors declare no competing financial interest.

Acknowledgment. The authors thank S. Gambino, M. Mazzeo, S. Patanè for helpful discussions and for having introduced us to squaraine-based microcavities, O. Maragò and A. Ridolfo for useful discussions and suggestions, and we thank A. Ridolfo also for help in the realization of Figure 1.

REFERENCES AND NOTES

1. Fofang, N. T.; Park, T.-H.; Neumann, O.; Mirin, N. A.; Nordlander, P.; Halas, N. J. Plexcitonic Nanoparticles: Plasmon-Exciton Coupling in Nanoshell-J-Aggregate Complexes. *Nano Lett.* **2008**, *8*, 3481–3487.
2. Ni, W.; Ambjo rnsson, T.; Apell, S. P.; Chen, H.; Wang, J. Observing Plasmonic-Molecular Resonance Coupling on Single Gold Nanorods. *Nano Lett.* **2010**, *10*, 77–84.
3. Ridolfo, A.; Di Stefano, O.; Fina, N.; Saija, R.; Savasta, S. Quantum Plasmonics with Quantum Dot-Metal Nanoparticle Molecules: Influence of the Fano Effect on Photon Statistics. *Phys. Rev. Lett.* **2010**, *105*, 263601.
4. Savasta, S.; Saija, R.; Ridolfo, A.; Di Stefano, O.; Denti, P.; Borghese, F. Nanopolaritons: Vacuum Rabi Splitting with a Single Quantum Dot in the Center of a Dimer Nanoantenna. *ACS Nano* **2010**, *4*, 6369–6376.
5. Manjavacas, A.; Abajo, F. G. a. d.; Nordlander, P. Quantum Plexcitonics: Strongly Interacting Plasmons and Excitons. *Nano Lett.* **2011**, *11*, 2318–2323.
6. Van Vlack, C.; Kristensen, P. T.; Hughes, S. Spontaneous Emission Spectra and Quantum Light-Matter Interactions from a Strongly Coupled Quantum Dot Metal-Nanoparticle System. *Phys. Rev. B* **2012**, *85*, 075303.
7. Alpeggiani, F.; D'Agostino, S.; Andreani, L. C. Surface Plasmons and Strong Light-Matter Coupling in Metallic Nanoshells. *Phys. Rev. B* **2012**, *86*, 035421.

8. Zengin, G.; Johansson, G.; Johansson, P.; Antosiewicz, T. J.; Käll, M.; Shegai, T. Approaching the Strong Coupling Limit in Single Plasmonic Nanorods Interacting with J-aggregates. *Sci. Rep.* **2013**, *3*, 3074.
9. DAgostino, S.; Alpeggiani, F.; Andreani, L. C. Strong Coupling between a Dipole Emitter and Localized Plasmons: Enhancement by Sharp Silver Tips. *Opt. Express* **2013**, *21*, 27602–27610.
10. Schlather, A. E.; Large, N.; Urban, A. S.; Nordlander, P.; Halas, N. J. Near-Field Mediated Plexcitonic Coupling and Giant Rabi splitting in Individual Metallic Dimers. *Nano Lett.* **2013**, *13*, 3281–3286.
11. Chen, X.-W.; Sandoghdar, V.; Agio, M. Coherent Interaction of Light with a Metallic Structure Coupled to a Single Quantum Emitter: From Superabsorption to Cloaking. *Phys. Rev. Lett.* **2013**, *110*, 153605.
12. Ozbay, E. Plasmonics: Merging Photonics and Electronics at Nanoscale Dimensions. *Science* **2006**, *311*, 189–193.
13. MacDonald, K. F.; Sámson, Z. L.; Stockman, M. I.; Zheludev, N. I. Ultrafast Active Plasmonics. *Nat. Photonics* **2008**, *3*, 55–58.
14. Chang, D. E.; Sørensen, A. S.; Demler, E. A.; Lukin, M. D. A Single-Photon Transistor Using Nanoscale Surface Plasmons. *Nat. Phys.* **2007**, *3*, 807–812.
15. Noginov, M.; Zhu, G.; Belgrave, A.; Bakker, R.; Shalaev, V.; Narimanov, E.; Stout, S.; Herz, E.; Suteewong, T.; Wiesner, U. Demonstration of a Spaser-Based Nanolaser. *Nature* **2009**, *460*, 1110–1112.
16. Hess, O.; Pendry, J.; Maier, S.; Oulton, R.; Hamm, J.; Tsakmakidis, K. Active Nanoplasmonic Metamaterials. *Nat. Mater.* **2012**, *11*, 573–584.
17. Schuller, J. A.; Barnard, E. S.; Cai, W.; Jun, Y. C.; White, J. S.; Brongersma, M. L. Plasmonics for Extreme Light Concentration and Manipulation. *Nat. Mater.* **2010**, *9*, 193–204.
18. Agio, M. Optical Antennas as Nanoscale Resonators. *Nanoscale* **2012**, *4*, 692–706.
19. Fofang, N. T.; Grady, N. K.; Fan, Z.; Govorov, A. O.; Halas, N. J. Plexciton Dynamics: Exciton- Plasmon Coupling in a J-Aggregate-Au Nanoshell Complex Provides a Mechanism for Nonlinearity. *Nano Lett.* **2011**, *11*, 1556–1560.
20. Vasa, P.; Wang, W.; Pomraenke, R.; Lammers, M.; Maiuri, M.; Manzoni, C.; Cerullo, G.; Lienau, C. Real-Time Observation of Ultrafast Rabi Oscillations between Excitons and Plasmons in Metal Nanostructures with J-Aggregates. *Nat. Photonics* **2013**, *7*, 128–132.
21. Haroche, S. Nobel Lecture: Controlling Photons in a Box and Exploring the Quantum to Classical Boundary. *Rev. Mod. Phys.* **2013**, *85*, 1083.
22. Auffeves, A.; Gerace, D.; Richard, M.; Portolan, S.; de Franca Santos, M.; Kwek, L. C.; Miniatura, C. *Strong Light-Matter Coupling: From Atoms to Solid-State Physics*; World Scientific Publishing Company: Singapore, 2013.
23. Bellessa, J.; Bonnand, C.; Plenet, J.; Mugnier, J. Strong Coupling between Surface Plasmons and Excitons in an Organic Semiconductor. *Phys. Rev. Lett.* **2004**, *93*, 036404.
24. Sugawara, Y.; Kelf, T.; Baumberg, J.; Abdelsalam, M.; Bartlett, P. Strong Coupling between Localized Plasmons and Organic Excitons in Metal Nanovoids. *Phys. Rev. Lett.* **2006**, *97*, 266808.
25. Hakala, T.; Toppari, J.; Kuzyk, A.; Pettersson, M.; Tikkanen, H.; Kunttu, H.; Törmä, P. Vacuum Rabi Splitting and Strong-Coupling Dynamics for Surface-Plasmon Polaritons and Rhodamine 6G molecules. *Phys. Rev. Lett.* **2009**, *103*, 053602.
26. Schwartz, T.; Hutchison, J. A.; Genet, C.; Ebbesen, T. W. Reversible Switching of Ultrastrong Light-Molecule Coupling. *Phys. Rev. Lett.* **2011**, *106*, 196405.
27. Guebrou, S. A.; Symonds, C.; Homeyer, E.; Plenet, J.; Gartstein, Y. N.; Agranovich, V. M.; Bellessa, J. Coherent Emission from a Disordered Organic Semiconductor Induced by Strong Coupling with Surface Plasmons. *Phys. Rev. Lett.* **2012**, *108*, 066401.
28. Tame, M.; McEnery, K.; Özdemir, Ş.; Lee, J.; Maier, S.; Kim, M. Quantum Plasmonics. *Nat. Phys.* **2013**, *9*, 329–340.
29. Niemczyk, T.; Deppe, F.; Huebl, H.; Menzel, E.; Hocke, F.; Schwarz, M.; Garcia-Ripoll, J.; Zueco, D.; Hümmer, T.; Solano, E.; *et al.* Circuit Quantum Electrodynamics in the Ultrastrong-Coupling Regime. *Nat. Phys.* **2010**, *6*, 772–776.
30. Todorov, Y.; Andrews, A. M.; Colombelli, R.; De Liberato, S.; Ciuti, C.; Klang, P.; Strasser, G.; Sirtori, C. Ultrastrong Light-Matter Coupling Regime with Polariton Dots. *Phys. Rev. Lett.* **2010**, *105*, 196402.
31. Scalari, G.; Maissen, C.; Turčinková, D.; Hagenmüller, D.; De Liberato, S.; Ciuti, C.; Reichl, C.; Schuh, D.; Wegscheider, W.; Beck, M.; *et al.* Ultrastrong Coupling of the Cyclotron Transition of a 2D Electron Gas to a THz Metamaterial. *Science* **2012**, *335*, 1323–1326.
32. Geiser, M.; Castellano, F.; Scalari, G.; Beck, M.; Nevou, L.; Faist, J. Ultrastrong Coupling Regime and Plasmon Polaritons in Parabolic Semiconductor Quantum Wells. *Phys. Rev. Lett.* **2012**, *108*, 106402.
33. Kéna-Cohen, S.; Maier, S. A.; Bradley, D. D. Ultrastrongly Coupled Exciton–Polaritons in Metal-Clad Organic Semiconductor Microcavities. *Adv. Opt. Mater.* **2013**, *1*, 827–833.
34. Mazzeo, M.; Genco, A.; Gambino, S.; Ballarini, D.; Mangione, F.; Di Stefano, O.; Patanè, S.; Savasta, S.; Sanvitto, D.; Gigli, G. Ultrastrong Light-Matter Coupling in Electrically Doped Microcavity Organic Light Emitting Diodes. *Appl. Phys. Lett.* **2014**, *104*, 233303.
35. Ridolfo, A.; Leib, M.; Savasta, S.; Hartmann, M. J. Photon Blockade in the Ultrastrong Coupling Regime. *Phys. Rev. Lett.* **2012**, *109*, 193602.
36. Ridolfo, A.; Savasta, S.; Hartmann, M. J. Nonclassical Radiation from Thermal Cavities in the Ultrastrong Coupling Regime. *Phys. Rev. Lett.* **2013**, *110*, 163601.
37. Stassi, R.; Ridolfo, A.; Di Stefano, O.; Hartmann, M.; Savasta, S. Spontaneous Conversion from Virtual to Real Photons in the Ultrastrong-Coupling Regime. *Phys. Rev. Lett.* **2013**, *110*, 243601.
38. De Liberato, S. Light-Matter Decoupling in the Deep Strong Coupling Regime: The Breakdown of the Purcell Effect. *Phys. Rev. Lett.* **2014**, *112*, 016401.
39. Borghese, F.; Denti, P.; Saija, R. *Scattering from Model Nonspherical Particles: Theory and Applications to Environmental Physics*; Springer: Berlin, 2007.
40. Chen, G.; Yokoyama, D.; Sasabe, H.; Hong, Z.; Yang, Y.; Kido, J. Optical and Electrical Properties of a Squaraine Dye in Photovoltaic Cells. *Appl. Phys. Lett.* **2012**, *101*, 083904.
41. Houdré, R.; Stanley, R.; Ilegems, M. Vacuum-Field Rabi Splitting in the Presence of Inhomogeneous Broadening: Resolution of a Homogeneous Linewidth in an Inhomogeneously Broadened System. *Phys. Rev. A* **1996**, *53*, 2711.
42. Johnson, P. B.; Christy, R.-W. Optical Constants of the Noble Metals. *Phys. Rev. B* **1972**, *6*, 4370.
43. Prodan, E.; Radloff, C.; Halas, N.; Nordlander, P. A Hybridization Model for the Plasmon Response of Complex Nanostructures. *Science* **2003**, *302*, 419–422.
44. Maier, S. A. *Plasmonics: Fundamentals and Applications*; Springer: Berlin, 2007.
45. Hopfield, J. Theory of the Contribution of Excitons to the Complex Dielectric Constant of Crystals. *Phys. Rev.* **1958**, *112*, 1555.
46. Quattropani, A.; Andreani, L.; Bassani, F. Quantum Theory of Polaritons with Spatial Dispersion: Exact Solutions. *Nuovo Cimento D* **1986**, *7*, 55–69.
47. Baumberg, J.; Heberle, A.; Kavokin, A.; Vladimirova, M.; Köhler, K. Polariton Motional Narrowing in Semiconductor Multiple Quantum Wells. *Phys. Rev. Lett.* **1998**, *80*, 3567.
48. Gambino, S.; Mazzeo, M.; Genco, A.; Di Stefano, O.; Savasta, S.; Patane, S.; Ballarini, D.; Mangione, F.; Lerario, G.; Sanvitto, G. G. Daniele Exploring Light–Matter Interaction Phe nomena under Ultrastrong Coupling Regime. *ACS Photonics* **2014**, *1*, 1042.
49. Nitsche, R.; Fritz, T. Determination of Model-Free Kramers-Kronig Consistent Optical Constants of Thin Absorbing Films from Just One Spectral Measurement: Application to Organic Semiconductors. *Phys. Rev. B* **2004**, *70*, 195432.
50. Bohren, C. F.; Huffman, D. R. *Absorption and Scattering of Light by Small Particles*; John Wiley & Sons: New York, 2008.

51. Ridolfo, A.; Saija, R.; Savasta, S.; Jones, P. H.; Iati, M. A.; Marago, O. M. Fano-Doppler Laser Cooling of Hybrid Nanostructures. *ACS Nano* **2011**, *5*, 7354–7361.
52. Rose, M. E. *Elementary Theory of Angular Momentum*; Courier Dover Publications: New York, 1995.
53. Jackson, J. D. *Classical Electrodynamics*, 2nd ed.; Wiley: New York, 1975.
54. Wyatt, P. J. Scattering of Electromagnetic Plane Waves from Inhomogeneous Spherically Symmetric Objects. *Phys. Rev.* **1962**, *127*, 1837.
55. Borghese, F.; Denti, P.; Saija, R.; Toscano, G.; Sindoni, O. Extinction Coefficients for a Random Dispersion of Small Stratified Spheres and a Random Dispersion of Their Binary Aggregates. *J. Opt. Soc. Am. A* **1987**, *4*, 1984–1991.